journal of the mechanical behavior of biomedical materials xxx (xxxx) xxx

Contents lists available at ScienceDirect

Journal of the Mechanical Behavior of Biomedical Materials

journal homepage: www.elsevier.com/locate/jmbbm

Research paper

Full-field microscale strain measurements of a nitinol medical device using digital image correlation

Kenneth I. Aycock [a,*], Jason D. Weaver [a], Harshad M. Paranjape [b], Karthikeyan Senthilnathan [b], Craig Bonsignore [b], Brent A. Craven [a]

[a] Division of Applied Mechanics, Office of Science and Engineering Laboratories, Center for Devices and Radiological Health, United States Food and Drug Administration, Silver Spring, MD 20993, United States of America

[b] Confluent Medical Technologies, Inc. 47533 Westinghouse Drive, Fremont, CA 94539, United States of America

ARTICLE INFO

Keywords:
Digital image correlation
Nitinol
Strain localization
Medical devices

ABSTRACT

Computational modeling and simulation are commonly used during the development of cardiovascular implants to predict peak strains and strain amplitudes and to estimate the associated durability and fatigue life of these devices. However, simulation validation has historically relied on comparison with surrogate quantities like force and displacement due to barriers to direct strain measurement–most notably, the small spatial scale of these devices. We demonstrate the use of microscale two-dimensional digital image correlation (2D-DIC) to directly characterize full-field surface strains on a nitinol medical device coupon under emulated physiological and hyperphysiological loading. Experiments are performed using a digital optical microscope and a custom, temperature-controlled load frame. Following applicable recommendations from the International DIC Society, hardware and environmental heating studies, noise floor analyses, and in- and out-of-plane rigid body translation studies are first performed to characterize the microscale DIC setup. Uniaxial tension experiments are also performed using a polymeric test specimen to characterize the strain accuracy of the approach up to nominal stains of 5%. Sub-millimeter fields of view and sub-micron displacement accuracies (9 nm mean error) are achieved, and systematic (mean) and random (standard deviation) errors in strain are each estimated to be approximately 1,000 $\mu\varepsilon$. The system is then demonstrated by acquiring measurements at the root of a 300 μm-wide nitinol medical device strut undergoing fixed-free cantilever bending motion. Lüders-like transformation bands are observed originating from the tensile side of the strut that spread toward the neutral axis at an angle of approximately 55°. Despite the inherent limitations of optical microscopy and 2D-DIC, simple and relatively economical setups like that demonstrated herein could provide a practical and accessible solution for characterizing cardiovascular implant micromechanics, validating computational model strain predictions, and guiding the development of next-generation material models for simulating superelastic nitinol.

1. Introduction

Digital image correlation (DIC) has been described as "the most important advance in experimental mechanics since the strain gage" (Reu, 2012). The method is a non-contact approach for extracting displacement and strain measurements from a sequence of digital images by correlating grayscale pixel intensities (Pan et al., 2009c; Sutton et al., 2009; Palanca et al., 2015; Pan, 2018). Building on advancements in computer vision and optical flow, the method was developed for the study of solid mechanics in the early 1980s at the University of South Carolina (Peters and Ranson, 1982; Sutton et al., 1983; Chu et al., 1985). Although initially limited to two-dimensional (2D) planar measurements of surface deformations at relatively large length scales, researchers have since extended the technique to the measurement of curved surfaces (single- and dual-camera stereo-DIC; Pan and Wang, 2013c; Li et al., 2017 and Sutton et al., 2008b,a, respectively), internal deformations (volumetric DIC; Bay et al., 1999), and micro- or even nano-scale mechanics using optical (Sun et al., 1997; Pitter et al., 2002; Quinta da Fonseca et al., 2005; Berfield et al., 2007; Sutton et al., 2008a; Jonnalagadda et al., 2009; Lei et al., 2010; Ya'akobovitz et al., 2010), scanning tunnel (Vendroux and Knauss, 1998), scanning electron (Davidson et al., 1983; Lagattu et al., 2006; Li et al., 2007; Jin et al., 2008; Winiarski et al., 2011; Kammers and Daly, 2013; Yan et al., 2015), and atomic force (Sun and Pang, 2006) microscopy. In brief,

* Corresponding author.
E-mail address: kenneth.aycock@fda.hhs.gov (K.I. Aycock).

https://doi.org/10.1016/j.jmbbm.2020.104221
Received 19 February 2020; Received in revised form 6 July 2020; Accepted 20 November 2020
Available online 23 November 2020
1751-6161/Published by Elsevier Ltd.

a standard subset-based 2D-DIC approach requires digital images with spatially varying grayscale intensity, ideally a non-repeating pattern of bright and dark patches referred to as a "speckle pattern". The reference image is discretized into a collection of "subsets", and possible subset deformations are described mathematically by a chosen set of shape functions. An optimization problem is then constructed to maximize the correlation in grayscale intensity values between subsets from the reference image and pixels in the deformed image, and displacement vectors are extracted. By using appropriate interpolation schemes, sub-pixel accuracies are routinely achieved (Pan et al., 2009c).

Given its ability to characterize full-field displacements and strains, DIC is attractive as a tool for validating computational solid mechanics models. Although strain gauges are also commonly used for this purpose, strain gauges require a direct bond to the surface of a specimen and therefore have the potential to influence measurements, whereas DIC is nominally a non-contact approach. Full-field DIC measurements also overcome the inherent spatial averaging associated with strain gauges and thereby mitigate the loss of fine-scale deformation details. Indeed, DIC has been used previously for validating finite element (FE) biomechanics models of femoral (Jetté et al., 2018), hemipelvic (Ghosh et al., 2012), craniofacial (Sutradhar et al., 2014), and dental (Tiossi et al., 2013) implants as well as replica (Dickinson et al., 2010) and cadaveric (Op Den Buijs and Dragomir-Daescu, 2011; Grassi et al., 2013) femurs. Digital image correlation has also been used to investigate the mechanics of polycrystalline nickel titanium (nitinol) starting in the mid 2000s (Murasawa et al., 2007; Daly et al., 2007), with interest rapidly increasing since that time (e.g., Reedlunn et al., 2011; Bewerse et al., 2013; Bechle and Kyriakides, 2014; Reedlunn et al., 2014; Bechle and Kyriakides, 2016; Zheng et al., 2016, 2017; Mazière et al., 2017; Jiang et al., 2017a; Zhang and He, 2018; Bian et al., 2019; Catoor et al., 2019; Paranjape et al., 2020). However, direct strain measurement on finished nitinol cardiovascular devices using either strain gauges or full-field DIC has been impractical to date due to limitations of scale, with typical strut cross-sectional dimensions measuring only a few hundred microns as illustrated in Fig. 1. Small scale DIC measurements have been performed on raw nitinol materials like plates and wires using scanning electron microscopy (Kimiecik et al., 2013; Gong and Daly, 2016), but such investigations require advanced setups. Because of the difficulty in acquiring direct strain measurements on implantable cardiovascular devices, computational models used for predicting device durability often rely on surrogate force–displacement experiments for validation. However, If computational predictions of strain are to be used to inform a high-risk decision, validating against such surrogate measurements may be inadequate (Pathmanathan et al., 2017; ASME V&V 40, 2018). Direct strain measurements are thus needed to enable more rigorous validation of computational models used to support the durability assessment of cardiovascular devices and to create opportunities for novel and higher-risk uses of evidence generated through computational modeling.

In this study, we overcome the following primary challenges to the application of microscale DIC to the characterization of nitinol cardiovascular device mechanics:

1. **setup complexity:** Images are acquired using a standard digital optical microscope, and speckle patterns are applied using finely ground carbon powder. Speckling requires little preparation and can be repeated by simply brushing away the electrostatically adhered powder and applying a new surface coating.
2. **need for temperature control**: Nitinol is an approximately equiatomic alloy of nickel and titanium that exhibits unique shape-memory and superelastic thermomechanical behavior. Because testing at physiological temperatures (approximately 37 °C) is critical when characterizing nitinol device mechanics, experiments are performed using a custom, temperature-controlled air environmental chamber designed to accommodate the small working distances typically required for high-magnification optical microscopy.
3. **limited depth of field**: An articulating base is used to carefully align specimens so that regions of interest are approximately perpendicular to the optical axis of the microscope objective during experiments. Measurements are acquired on laser-cut surfaces of the device that are made planar by high-quality electropolishing.

Using this setup, we characterize the error associated with our DIC method by following relevant recommendations from the International DIC Society's recent publication "A Good Practices Guide for Digital Image Correlation" (Jones and Iadicola, 2018) and from previous 2D-DIC work (Pan et al., 2013d). Error characterization tests include camera and hardware heating studies, displacement and strain noise floor characterization, in-plane and out-of-plane rigid body translation studies, and uniaxial tension experiments. Finally, we demonstrate the method on a nitinol cardiovascular device coupon specimen with a strut width of approximately 300 μm.

2. Materials and methods

2.1. Experimental setup

Experiments are performed on a vibration isolation table (Benchmate 2200 series, Kinetic Systems) using a digital optical microscope (KH770, HIROX) and a custom temperature-controlled load frame (Fig. 2a). An articulating base (AP-180, Thorlabs) is also used in some experiments (Fig. 2a). The microscope is configured for reflected bright-field illumination (coaxial) provided by a halogen light source. Digital images are captured by a two megapixel charge-coupled device (CCD) sensor and are stored as 8-bit lossless grayscale TIFF files. Magnification is provided by an MXG-2500 REZ triple objective turret with a working distance of 10 mm. For all images considered here, the high-range lens is used at a medium zoom level corresponding to 500× magnification, yielding an effective image spatial resolution of 0.37 μm/pixel.

The miniature load frame (Fig. 2b) consists of a temperature-controlled breadboard (PTC1, Thorlabs), a high-precision linear actuator with a non-rotating spindle (M-230.25, Physik Instrumente), a 200-gram load cell (LSB200, Futek), two thermistors (TSP-TH, Thorlabs, Inc.), a 12 VDC brushless fan, 3/8 inch thick acrylic sidewalls topped with adhesive foam padding, and a 1/16 inch thick acrylic chamber cover plate (Fig. 2b). A 1.25 inch diameter hole through the chamber cover allows for passage of the objective into the heated air chamber (Fig. 2a), thus facilitating image capture at the short working distances typically required for high-magnification microscopy.

As needed, temperature management is provided by a proportional–integral–derivative (PID) controller through software from Thorlabs. One thermistor is placed in contact with the temperature-sensitive test specimen and connected to the input of the PID controller. A second thermistor is suspended in the air a few millimeters from the test specimen to monitor spatial temperature gradients by evaluating the temperature difference between the two thermistor measurements (Fig. 2b, ⑨). The breadboard-mounted fan is also powered on and used during temperature-controlled experiments to mix the air throughout the air chamber to minimize temperature gradients.

Three specimens are used in the 2D-DIC error characterization and demonstration experiments (Fig. 3). Camera heating effects, noise floor estimation, and in- and out-of-plane rigid body translation errors are characterized using a flat, 1 cm × 1 cm × 500 μm electropolished nitinol strip adhered to an aluminum right angle bracket using cyanoacrylate (Fig. 3a). A hole in the angle bracket allows for the specimen to be mounted directly to the spindle of the digital actuator. Because nitinol cannot be easily subjected to *uniform* strain beyond 1% due to material instability and localization phenomena, strain error quantification experiments are instead performed using a polymeric strip of Tygon tubing laminated between acrylic end pieces (Fig. 3b). A thin specimen is used to reduce out-of-plane motion generated by Poisson contraction in the through-plane axis during extension (e.g., as noted in Quinta da

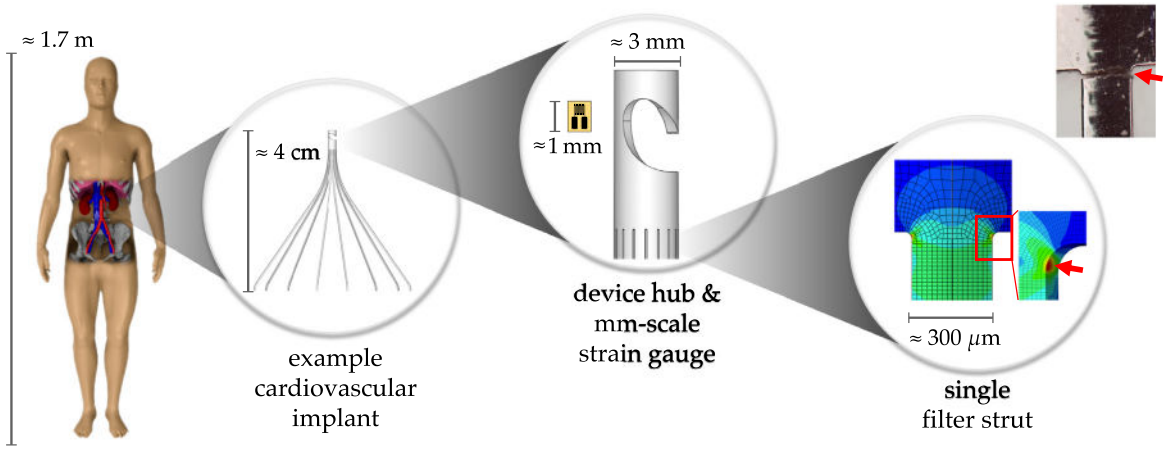

Fig. 1. Spatial scales relevant to implantable cardiovascular devices. The smallest strain gauges currently manufactured are millimeter-scale, whereas parameters of interest for fatigue assessment (e.g., peak strains and strain amplitudes) occur on spatial scales on the order of microns or smaller.

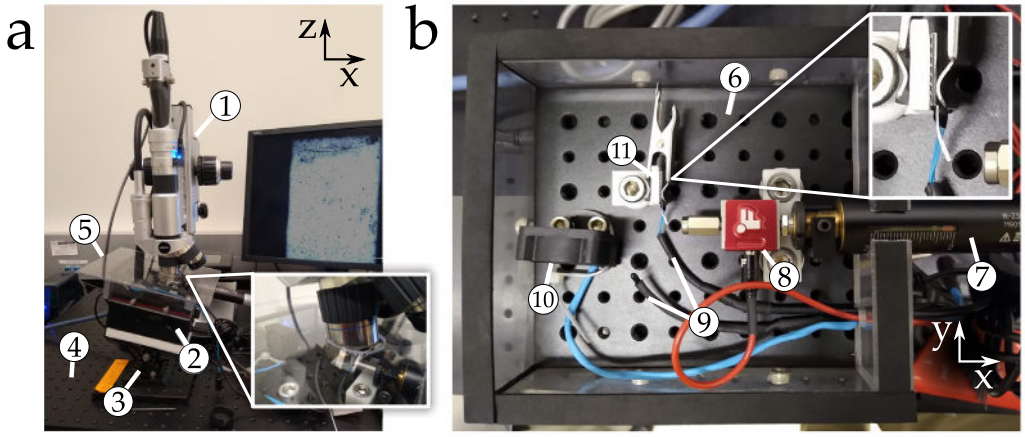

Fig. 2. (a) Microscope and miniature temperature-controlled load frame used in the microscale 2D-DIC experiments. (b) Enlarged view of the miniature load frame. ①: far-field digital optical microscope, ②: miniature load frame, ③: articulating base, ④: vibration isolation table, ⑤: chamber cover plate, ⑥: heated breadboard, ⑦: precision digital micrometer with non-rotating spindle, ⑧: miniature load cell, ⑨: thermistors for temperature control and monitoring, ⑩: fan used to circulate air in the chamber, ⑪: angle bracket, clamp, and nitinol device coupon specimen.

Fonseca et al., 2005), thus reducing the need for refocusing during experiments. Demonstration experiments are performed using a nitinol coupon specimen representing a single strut of a generic nitinol (GENI) inferior vena cava (IVC) filter designed by the authors (Fig. 3c). The coupon specimen was manufactured at Confluent Medical Technologies (Fremont, CA) by laser cutting the geometry from 2.032 mm diameter SE508 (50.8 at.% nickel) nitinol tubing, shape setting the strut profile, and electropolishing the surface. Based on differential scanning calorimetry (DSC) measurements (Duerig et al., 2017), the finished coupons have a martensite reversion peak temperature $M_p^* = 13\,°C$, an R-phase reversion peak temperature $R_p^* = 23\,°C$, and an austenite finish temperature $A_f = 30\,°C$.

All specimens are speckled with a polydisperse carbon powder using the procedure shown in Fig. 4. Note that the approach uses the native specimen surface as the background for the speckles in lieu of applying a base coat of paint. Similar techniques were previously performed for microscale DIC using silicon microparticles (Gianola, 2007; Jonnalagadda et al., 2009). Specimens are first cleaned as needed by immersing them in a solution of acetone and deionized water (50/50 by volume) within a centrifuge tube and sonicating (M series, Branson) the tubes for 15 min. After removal and drying, specimens are reinserted into centrifuge tubes containing finely ground activated carbon powder (Fig. 4a, i), shaken (Fig. 4a, ii), and then separated from the powder using a sieve screen and nonmarring plastic tweezers.

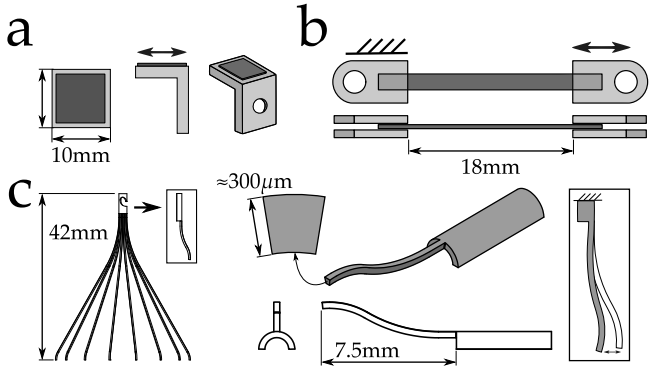

Fig. 3. Specimens used in the microscale 2D-DIC error characterization and demonstration experiments with approximate dimensions. (a) Electropolished nitinol strip adhered to an aluminum right-angle bracket for noise floor characterization and rigid body motion experiments. (b) Polymer band specimen laminated between acrylic sheets at the ends for strain error characterization experiments under approximately uniform uniaxial tension. (c) Nitinol coupon specimen representative of a generic IVC filter designed by the authors.

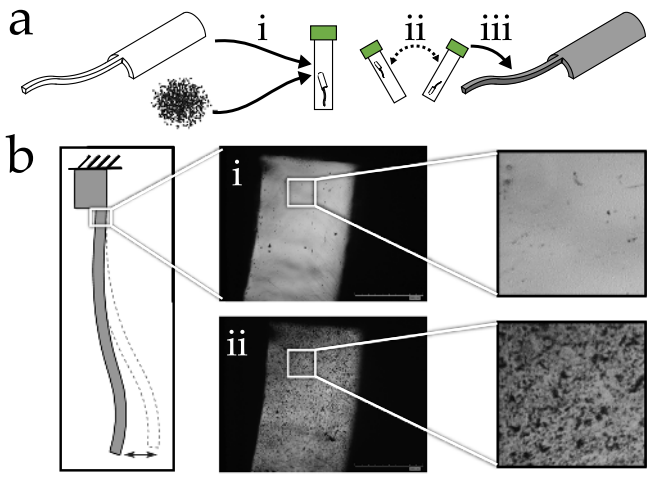

Fig. 4. (a) Speckling approach used in our 2D-DIC experiments. Samples are (i) inserted into a centrifuge tube containing finely-ground carbon powder, (ii) shaken, and (iii) removed. Although speckles are not visible to the naked eye, samples appear slightly darker after speckling. (b) Representative micrographs of samples (i) before and (ii) after speckling.

Upon removal, speckles are invisible to the naked eye, although some discoloration is apparent (Fig. 4a). Micrographs at 500× magnification reveal the presence of opaque carbon particles (Fig. 4b, ii) adhering to the nitinol surface via electrostatic forces (Gianola, 2007; Jonnalagadda et al., 2009). Finally, large particles and particle aggregates are blown away using a bulb syringe (similarly to Gianola, 2007). Although rigid particles like those used herein violate the assumption in DIC algorithms that speckle deformations exactly track the underlying specimen deformations, Barranger et al. (2012) previously demonstrated errors associated with rigid particle speckle patterns are unbiased (random) and comparable to the image noise errors still present using ideal deformable particles, even for imposed Green–Lagrange strains as high as 80%. Inspection under microscopy also confirms that particles electrostatically adhere to the specimen surface and faithfully follow underlying material deformations.

Speckle patterns are quantitatively characterized using two metrics: mean speckle size (Lecompte et al., 2006) and mean intensity gradient (Pan et al., 2010a). Mean speckle size is estimated in `ImageJ` (Schneider et al., 2012) by performing local contrast enhancement, converting images to binary by application of a pixel intensity threshold, applying a watershed filter to separate partially overlapping speckles, and finally using the '`analyze particles`' tool to extract mean speckle diameters and areas. Mean intensity gradient (MIG) is calculated in `Python/NumPy` using the central-difference-based gradient function. Using this approach, the mean speckle diameter and area are found to be approximately 5 pixels and 30 pixels^2, respectively, for all specimens. Mean intensity gradients range from approximately 11 for the polymer band specimens to 17 for the nitinol strip and coupon specimens and are comparable to the MIGs previously reported for macroscale speckle patterns generated using aerosol paints (12 to 35; Pan et al., 2010a).

2.2. DIC processing

Surface displacements and strains are extracted from image sequences using the open-source subset-based 2D-DIC software `Ncorr-C++` (Blaber et al., 2015). `Ncorr-C++` uses the recently developed reliability-guided approach (RG-DIC Pan, 2009a) to increase the speed of computation and to decrease the risk for failing to find a match between reference and deformed images (decorrelation). The procedure first chooses a seed subset in the reference image and identifies a match in the deformed image by optimizing the correlation criteria. After the deformation of the seed subset has been determined, neighboring subsets are selected and initialized using the displacement results from the seed subset. The process is repeated for all subsequent computations by updating the reference displacement to that from the nearest subset neighbor. In so doing, fewer iterations are needed to optimize the correlation, greatly decreasing computation time and preventing the need for an exhaustive search over all image space. `Ncorr-C++` additionally leverages the inverse compositional Gauss–Newton (IC-GN) approach (Pan et al., 2013b) as the nonlinear optimizer for sub-pixel accuracy. `Ncorr-C++` was previously verified using the Society of Experimental Mechanics 2D-DIC Challenge Data (Blaber et al., 2015; Reu et al., 2018) and by comparison with results from the commercial code VIC-2D (Harilal et al., 2014).

For the DIC analyses performed herein, a region of interest (ROI) is first defined using a black-and-white TIFF image mask. The ROI is $446 \times 297\ \mu m^2$ for the nitinol strip and polymer band specimens, and $241 \times 303\ \mu m^2$ for the nitinol coupon. To reduce interpolation bias and aliasing (Pan, 2013a; Su et al., 2015), Gaussian pre-filtering of images is performed in `Python/OpenCV` (Bradski, 2000) using a 3×3 kernel and a sigma value of 0.8. The filtered images are analyzed in `Ncorr-C++` using circular subsets with a radius of 31 pixels, a step size ('`scalefactor`' in `Ncorr-C++`) of 5 pixels, and a correlation coefficient cutoff of 2. After extracting displacements, Green–Lagrange strains are calculated in `Ncorr-C++` by differentiating the displacement field using the pointwise least squares strain window smoothing algorithm (Pan et al., 2009b) and a strain window radius of 10 subsets. Displacement and strain results are finally exported as comma-separated values (CSV) files and read by `Python` for further visualization and post-processing. With the selected DIC processing parameters, 7800 (demonstration experiments) to 38,400 (DIC error characterization experiments) displacement and strain measurements are extracted from each image pair.

Details on the imaging, lighting, and sensors used in the DIC experiments and parameters used in the DIC processing are summarized in Table 1.

2.3. 2D-DIC error characterization experiments

To characterize errors associated with our specific experimental setup, we follow relevant recommendations from Section 3, "Preparation for the Measurements", of the iDICs good practices guide (Jones and Iadicola, 2018). Because DIC measurements are sensitive to many environmental factors, including ambient temperature, vibrations, and lighting, and to application-specific speckle pattern quality, error characterization tests like those that follow (or a subset thereof) are typically recommended prior to initiating a new DIC study. Note that the iDICs guide explicitly states it does not cover additional considerations for advanced setups such as those using microscopy. Thus, some of our methodology deviates from the iDICs recommendations. For example, although the iDICs guide recommends no changes be made to the camera setup once experiments begin, adjustment of the stand-off distance is sometimes required for microscale measurements (e.g., Sun et al., 1997; Pitter et al., 2002; Lei et al., 2010) to mitigate defocusing errors that occur with even subtle out-of-plane motion due to the limited depth of field at high magnifications. Therefore, refocusing is performed as needed throughout the experiments described herein.

2.3.1. Camera and hardware heating study

Previous studies (Pan et al., 2013d; Yu et al., 2019; Zhou et al., 2020) have shown hardware self-heating to influence DIC measurements due to thermal expansion in the camera sensors and associated components (e.g., lenses and mirrors). As such, iDICs recommends waiting for all hardware to reach a steady-state temperature prior to acquiring images (Section 3.1.3 in Jones and Iadicola, 2018). Here, the influence of camera and hardware heating is quantified by tracking mean displacements and strains over time while imaging a static sample

Table 1
Description of the microscale 2D-DIC setup reported as recommended in Reu (2015).

Imaging system	HiRox KH7700 digital optical microscope
Sensor	2 MP CCD, 8-bit
Image size	1600 × 1200 pixels
Lens	HiRox MXG-2500 REZ, high range
Light source	60 W metal halide lamp
Magnification	500×
Working distance	10 mm
Light configuration	Bright-field, coaxial
DIC software	`Ncorr-C++` (open-source) (Blaber et al., 2015)
Previous verification	Comparison to Society of Experimental Mechanics 2D-DIC Challenge Data (Reu et al., 2018; Blaber et al., 2015)
Spatial scale	0.37 μm / pixel
Speckle background	Electropolished nitinol surface
Speckle foreground	Finely ground activated carbon powder
Mean speckle size	≈30 pixels^2
Image filtering	Low-pass (3 × 3 kernel Gaussian)
Subset shape and size	Circular, 31 pixel radius
Strain window shape and size	Circular, 10 subset radius
Step size	5 pixels
Subset advancement	Reliability guided (RG) (Pan, 2009a)
Initial cross correlation	Zero-mean normalized cross correlation (ZNCC) (Pan et al., 2010b)
Final cross correlation	Zero-mean normalized sum of squared difference (ZNSSD) (Pan et al., 2010b)
Nonlinear optimizer	Inverse compositional Gauss–Newton (IC-GN) (Pan et al., 2013b)
Interpolation	Biquintic B-spline

to estimate the required waiting time for the system to reach a thermal steady-state.

Experiments are performed using the nitinol strip specimen from Fig. 3a. The specimen is mounted to the micrometer spindle using an M4 set screw and nut. The experiment is initialized with the microscope turned off for two or more hours (i.e. "cold"). The load frame is positioned under the microscope and the microscope is powered on. Time-lapse image acquisition of the nominally static specimen then begins as soon as the specimen is brought into focus and rotated so that the specimen plane is approximately perpendicular to the optical axis of the microscope. Images are taken every two minutes for a three-hour period. Note that the heated breadboard and fan are not powered during this study. Following the experiment, images are processed in `Ncorr-C++` and spatially averaged displacements and strains are calculated and plotted versus elapsed time.

2.3.2. Noise floor characterization and DIC parameter sensitivity study

To characterize the influence of random image noise on the DIC results (Section 3.3.1.3 in Jones and Iadicola, 2018), images are acquired of the nominally static nitinol strip specimen (Fig. 3a) after allowing the camera and hardware to heat for the determined warm-up time (100 min). Two images are acquired in rapid succession of the nominally static specimen, once at room temperature and a second time with the heated breadboard and fan powered on and the PID control loop set to and stabilized at 37 °C. This second test is used to investigate the influence of environmental heating on the measurement noise floor. Images are processed in `Ncorr-C++` to extract the systematic (mean) and random (standard deviation) errors in the displacement and strain fields.

We additionally perform a DIC parameter sensitivity study using the nominally static room-temperature image pair. Specifically, the two parameters that have the greatest influence on measurement noise floor in `Ncorr-C++`, the subset and strain window size, are varied over representative ranges (subset radii of 21, 31, and 41 and strain window radii of 5, 10, and 20). The resulting systematic and random strain errors are then quantified for each permutation of these parameters. Note the inherent trade-off between spatial resolution and measurement noise when selecting these parameters (see Section 5.4.4 in Jones and Iadicola, 2018). By investigating the sensitivity of the measurements to user-selected DIC parameters, as we do here, the suitability of the chosen parameters can be assessed based on the noise tolerance and spatial resolution requirements for the application of interest.

2.3.3. Out-of-plane rigid body translation study

Out-of-plane motion of specimens has previously been reported as a primary source of error for 2D-DIC measurements (Sutton et al., 2008b; Pan et al., 2013d). In the context of microscale DIC, out-of-plane errors have also been referred to as "refocus errors" (Sun et al., 1997) given that refocusing the microscope by adjusting the stand-off distance of the objective is frequently required to keep a specimen in focus during an experiment, and any error in matching the original stand-off distance will generate measurement errors. Because of the importance of out-of-plane motion errors for 2D-DIC, the iDICs guide recommends characterizing the magnitude of these errors in response to the range of out-of-plane motions that may occur during an experiment (Section 3.3.1.5 and Recommendation 3.15 in Jones and Iadicola, 2018).

Here, we estimate out-of-plane errors by first acquiring a reference image of a nominally static specimen in sharp focus (Fig. 3a). Images are then acquired with the motorized objective moved to the lower ($\approx -3\mu m$) and upper ($\approx +3\mu m$) bounds of the depth of field where blurring of the images becomes qualitatively obvious. Images are again processed in `Ncorr-C++` to extract the systematic (mean) and random (standard deviation) errors in the displacement and strain fields.

2.3.4. In-plane rigid body translation study

In-plane rigid body translation tests have been used since the earliest DIC studies (e.g., Peters and Ranson, 1982) to characterize displacement accuracy and are recommended by the iDICs guide for this same purpose (Section 3.3.15 Jones and Iadicola, 2018). Errors computed from in-plane translation tests represent a combination of the errors generated by spatially varying lens distortion, illumination, and camera sensor noise. Lens distortion errors are especially important to characterize when performing high-magnification optical microscopy as we do here.

We characterize the displacement accuracy of our DIC system by translating the nitinol strip specimen (Fig. 3a) along one axis using the M-230.25 precision actuator that has a nominal sensor resolution of 5 nm and a minimum increment resolution of 50 nm. To avoid backlash, the actuator is first advanced a few millimeters in the target direction of travel before acquiring a reference image. Total displacements of 1, 2, 5, 10, 20, and 50 μm are then prescribed, with an image taken after each displacement increment.

Images are processed in `Ncorr-C++` to extract displacements and strains. Systematic (mean) errors in displacement are calculated by computing the mean difference between the measured and nominal displacement over each subset, and random errors are calculated by computing the standard deviation of the displacement field (nominally zero). Systematic (mean) and random (standard deviation) errors in the nominally zero strain field are also calculated from the subset values.

2.3.5. Uniaxial tension test

In addition to the tests recommended by the iDICs guide, we also perform a uniaxial tension test as in Sun et al. (1997) and Pan et al. (2013d) to characterize the accuracy of strain measurements with our DIC setup. For these experiments, the articulated base is removed, and the load frame is placed upon the motorized stage of the KH7700 microscope. The polymer specimen (Fig. 3b) is fastened in the air

chamber between a #8 eye bolt (fixed end) and a 4 mm miniature clevis mount (actuated end). To prevent sagging, a small pre-strain is applied to the specimen, and the reference length L is recorded along with a reference image. Deformed lengths l needed to prescribe uniaxial Green–Lagrange strains $\epsilon_G = \frac{1}{2}\left(\frac{l^2}{L^2} - 1\right)$ of 1%, 2%, 3%, 4%, and 5% are then calculated and prescribed by moving the actuator, and deformed images are acquired at each nominal strain level. To keep the original ROI approximately centered in the field of view, the load frame is repositioned after each increment in strain using the motorized stage.

Images are processed in `Ncorr-C++` to extract strains. Systematic (mean) errors in strain are calculated by computing the mean difference between the measured and nominal strains at each subset, and random errors are calculated by computing the standard deviation of the measured strain field.

2.4. Nitinol device coupon demonstration experiments

Use of the characterized microscale 2D-DIC system is demonstrated on a nitinol medical device coupon under emulated physiological and hyperphysiological loading. Specifically, the single-strut nitinol IVC filter coupon specimen (Fig. 3c) is subjected to fixed-free cantilever bending motion by clamping the coupon hub and pressing on the distal end of the strut using a flat micrometer tip (Fig. 3c, right). The miniature force transducer is placed inline between the micrometer and the specimen for these experiments (Fig. 2b). Because the mechanics of nitinol are highly temperature-dependent, experiments are performed at body temperature (37 °C) using the previously described temperature control loop.

For these experiments, the ROI is the sidewall of the strut at the strut root (Fig. 4b) where the highest strains occur during bending. Because the nitinol coupon is laser cut from round tubing, the strut sidewalls are not parallel to one another or to the load frame base (Fig. 3c). Thus, to allow for alignment of the ROI to the camera viewing plane, the miniature load frame is mounted on the articulating platform for these experiments (Fig. 2a, ③). The platform is tilted and the microscope objective adjusted until as much of the coupon sidewall is in focus as possible. After aligning and focusing the microscope, a reference image is acquired of the strut sidewall in the undeformed configuration. The coupon is then subjected to quasi-static loading as the strut tip is displaced in increments of 0.163 mm up to a maximum displacement of 2.61 mm and then unloaded by the same increments, with images and forces recorded at each displacement level. The micrometer is translated at a relatively slow rate of approximately 0.05 mm per second to minimize temperature changes in the nitinol associated with the latent heat of crystallographic phase transformation between cubic (B2) austenite and monoclinic (B19') martensite.

3. Results

3.1. 2D-DIC error characterization experiments

Results of the error characterization tests are summarized in Table 2.

3.1.1. Camera and hardware heating study

Images acquired from an initially cool (i.e., room-temperature) system reveal a settling period during which displacements and false strains in the DIC results increase in magnitude (Fig. 5). Interrogation of raw images and extracted displacements reveals evidence of in-plane spatial drift, with final displacement magnitudes of about 3–4 μm in both the x- and y-directions at the end of the three-hour study (Fig. 5, left). The observed mean ϵ_{xx} and ϵ_{yy} strains first increase slightly ($0 < t < 2$ min), then decrease sharply until reaching a minimum of approximately $-3000\,\mu\epsilon$ at $t = 100$ min (Fig. 5, right). From $t = 100$ min on, the ϵ_{xx} and ϵ_{yy} strains remain approximately constant, indicating that a steady state has been reached. In contrast, the mean shear strain ϵ_{xy} remains approximately unchanged throughout the experiment (Fig. 5, right). Image focus also deteriorates during the initial settling-in period between $0 < t < 100$ min.

3.1.2. Noise floor characterization and DIC parameter sensitivity study

Images of nominally static samples taken after the 100 min hardware warm-up period are used to estimate the systematic and random errors in displacement and strain as summarized in Table 2. Images taken at room temperature and with environmental heating to 37 °C yield very similar displacement and strain noise levels (Table 2; Fig. 6a). Under these nominally static conditions, the one-standard deviation strain noise floor is comparable in the ϵ_{xx} and ϵ_{yy} strains, both with and without environmental heating, and is estimated to be approximately $250\,\mu\epsilon$ (Table 2; Fig. 6a).

The DIC parameter sensitivity study reveals systematic errors are relatively insensitive to subset or strain window size over the explored parameter space, whereas random strain errors vary nearly an order of magnitude (Fig. 6b). Larger subset and strain window sizes are observed to generate smaller random strain errors, although at the cost of the effective spatial resolution (Fig. 6b). Computation times also vary inversely with subset size, ranging from 148 points per second per processor for a subset radius of 41 pixels to 394 points per second per processor for a subset radius of 21 pixels.

3.1.3. Out-of-plane rigid body translation study

Out-of-plane translations to the upper and lower bounds of the depth of field generate relatively large errors in both displacement and strain compared to those observed with a static sample in sharp focus (Table 2; Fig. 7). Mean strain errors are positive ($\approx +2000\,\mu\epsilon$) when the objective is moved away from the specimen ($z+$) and negative ($\approx -1500\,\mu\epsilon$) when the objective is moved toward the specimen ($z-$) (Fig. 7, left). The estimated strain noise floor is approximately 2.7 × higher than that observed in the absence of intentionally applied out-of-plane motion (Table 2; Fig. 7, right).

3.1.4. In-plane rigid body translation study

Excellent agreement is observed between nominal actuator displacements and those measured using 2D-DIC (Table 2; Fig. 8). The mean displacement error is approximately 9 nm (Table 2). Random errors in displacement are relatively small for small displacements (e.g., standard deviation $\sigma = 34$ nm at 1 μm displacement) and increase with increasing displacement (standard deviation $\sigma = 411$ nm at 50 μm displacement; Fig. 8). Systematic and random errors in strain are greater than those obtained from the noise floor characterization study but less than those observed during the out-of-plane translation experiments (Table 2).

3.1.5. Uniaxial tension test

Excellent agreement is also observed between nominal uniaxial strains and those measured by 2D-DIC in experiments using the polymer band specimen (Table 2; Fig. 9). Overall, the systematic (mean) strain error is approximately $-912\,\mu\epsilon$, and the systematic errors are lower at small strains (e.g., $-159\,\mu\epsilon$ error at $10{,}000\,\mu\epsilon$) than at larger strain levels (e.g., $-2154\,\mu\epsilon$ error at $50{,}000\,\mu\epsilon$; Fig. 9). Random errors also increase over the explored strain range from $750\,\mu\epsilon$ error at $10{,}000\,\mu\epsilon$ to $2052\,\mu\epsilon$ error at $50{,}000\,\mu\epsilon$ (Fig. 9).

3.2. Nitinol device coupon demonstration experiments

Fixed-free cantilever bending experiments on the nitinol coupon specimens (Fig. 10a) reveal nonlinear force–displacement behavior (Fig. 10b) and hysteresis between the loading and unloading paths for tip displacements greater than approximately 0.8 mm (points ④–⑮; Fig. 10b). Full-field strain measurements acquired on the sidewall of the strut root show typical continuous strain contours for beam bending up

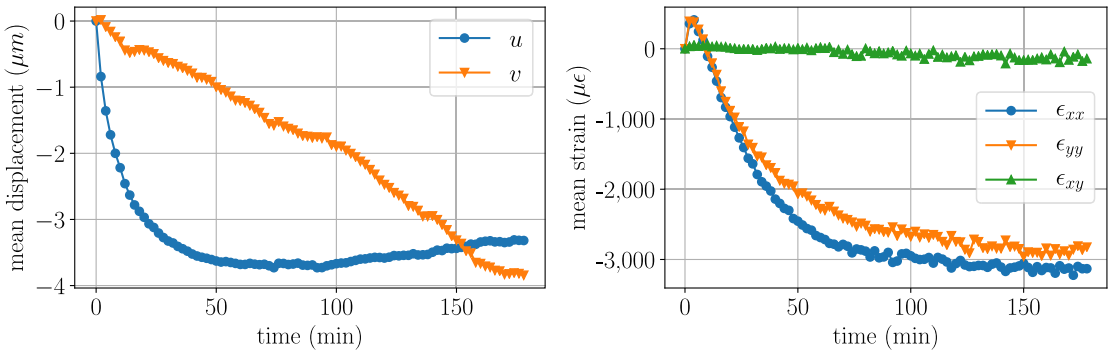

Fig. 5. Spatial drift (left) and false strains (right) versus elapsed time from the three-hour camera and hardware heating study. An approximately steady state is reached after 100 min in all fields except the y-displacement (v). All strains are Green–Lagrange.

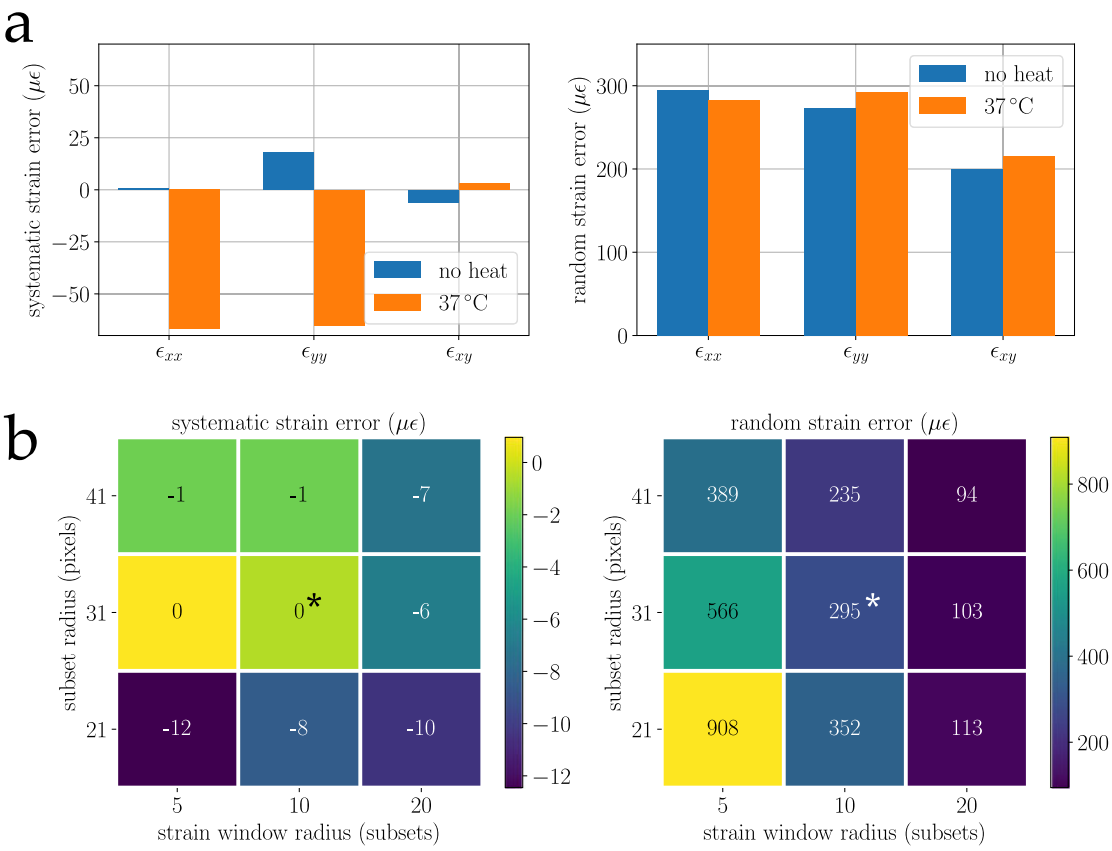

Fig. 6. (a) Systematic (mean) and random (standard deviation) strain errors extracted from two subsequent images of a nominally static sample. Random errors are represented by one standard deviation. (b) Strain errors (ϵ_{xx}) extracted from the same room-temperature static image pair for varied DIC processing parameters (subset and strain window radii). Parameters used elsewhere throughout the study are those at the center of the explored parameter space (asterisks).

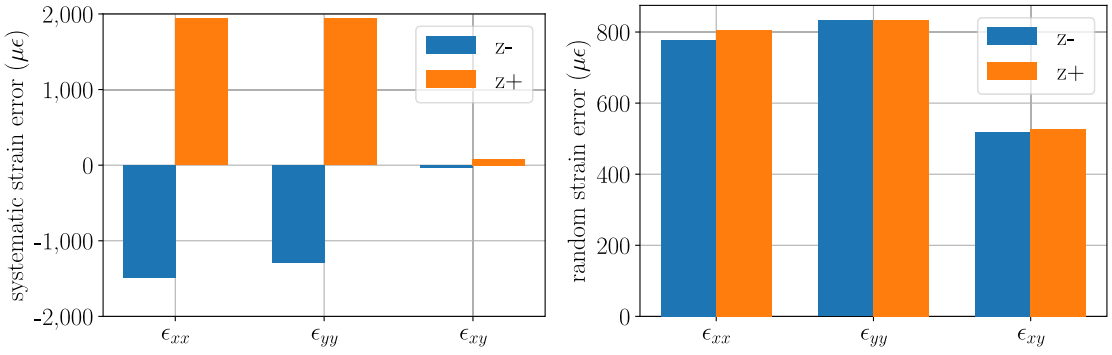

Fig. 7. Systematic (mean) and random (standard deviation) strain errors generated by out-of-plane translations of the objective lens toward ($z-$) and away from ($z+$) a nominally static specimen initially in sharp focus. Translations are large enough to appreciably deform the image. Random errors are represented by one standard deviation.

Table 2
Estimated errors in displacement and strain from microscale 2D-DIC error characterization experiments.

	Static		Static, 37 °C		Rigid body, out-of-plane		Rigid body, in-plane		Uniaxial strain	
Error	syst. (mean)	rand. (std)	syst. (mean)	rand. (std)	syst. (mean)	rand. (std)	syst. (mean)	rand. (std)	syst. (mean)	rand. (std)
μm	−0.032	0.007	−2e−5	1.1e−4	0.176	0.188	0.009	0.109	N/A	N/A
$\mu\epsilon$	4	256	−43	264	*1130	716	758	402	−912	1162

syst: systematic error; rand: random error; std: standard deviation; N/A: not applicable.
*Average absolute value of mean strains generated by out-of-plane translation (i) toward and (ii) away from the specimen.

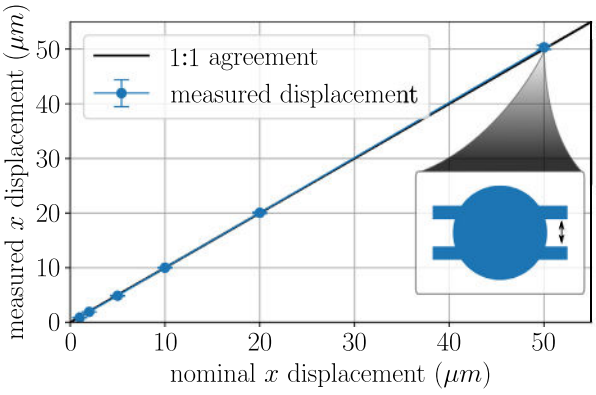

Fig. 8. Results from in-plane rigid body displacements of a planar nitinol specimen for displacement error characterization. Error bars represent one standard deviation of the displacements extracted from the region of interest. The inset of the data point at a nominal displacement of 50 μm shows the relatively small size of the error bars relative to the vertical axis.

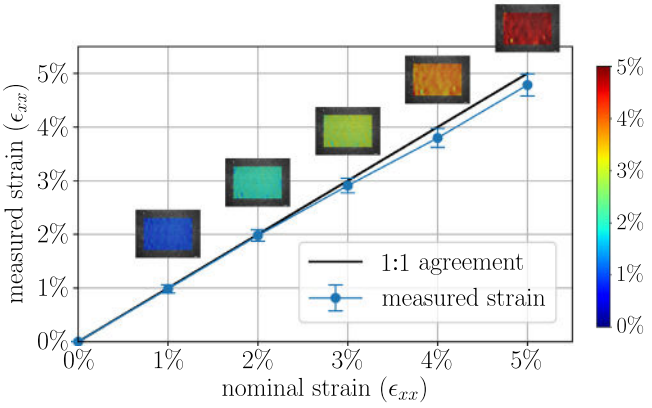

Fig. 9. Results from uniaxial tension experiments with a polymer band specimen between nominal strains of 10,000 με (1%) and 50,000 με (5%). Error bars represent one standard deviation of the calculated strain values over the DIC region of interest. All strains are Green–Lagrange.

to tip displacements of approximately 1.3 mm (frames ①–⑤; Fig. 10c). Above tip displacements of 1.3 mm, Lüders-like transformation bands initiate and spread from the tensile side toward the neutral axis (frames ⑥–⑨; Fig. 10c). Transformation bands persist upon unloading until the tip displacement decreases below 1.3 mm (frames ⑩–⑭; Fig. 10c). Localization bands then begin to recede (frame ⑭) until they are no longer visible below tip displacements of approximately 0.65 mm (frames ⑯–⑱; Fig. 10c). After mapping the full-field strain results for maximal tip displacement (frames ⑨ and ⑩) to the reference configuration, the angle between the transformation bands and the strut axis is measured to be approximately $\alpha = 54.9 \pm 3°$ (Fig. 10d).

4. Discussion

Building upon previous 2D-DIC studies using bright-field microscopy (e.g., Sun et al., 1997; Quinta da Fonseca et al., 2005; Lei et al., 2010), we demonstrate the use of a standard digital optical microscope and a low-cost temperature-controlled miniature load frame to acquire full-field surface measurements over sub-millimeter fields of view with sub-micron displacement accuracy. Microscale full-field measurements like those demonstrated herein have not been reported previously for finished cardiovascular medical devices. Such measurements may be used by device engineers to more directly validate and improve the computational models they use for device development. Full-field measurements will also guide the development and validation of models capable of reproducing inhomogeneous deformations (Shaw and Kyriakides, 1997; Hallai and Kyriakides, 2013; Jiang et al., 2017b) like the strain localization bands observed herein (Fig. 10). Measurements of medical devices undergoing emulated physiological loading may additionally be useful for detecting cyclic crystallographic phase transformation, which has recently been demonstrated to be an indicator for low-cycle fatigue failure (Catoor et al., 2019; Paranjape et al., 2020). While more advanced methods such as high-energy X-ray diffraction can provide a more direct measure of the phase transformation (e.g., Paranjape et al., 2017) in bulk samples such as medical devices, the 2D-DIC method described here provides access to similar information with a substantially simpler experimental setup.

Where applicable, we follow recommended good practices from iDICs (Jones and Iadicola, 2018) to characterize our 2D-DIC setup and estimate measurement errors in displacement and strain. Camera and hardware heating studies reveal a required warm-up time of approximately 100 min to reach steady-state operation (Fig. 5), similar to previous macroscale studies (e.g., approximately 1.5 hr in Pan et al., 2013d). Random (standard deviation) errors estimated from image pairs taken of a static sample are also comparable to those reported in previous studies (e.g., ≈ 0.02 pixels here and in Sun et al., 1997; Lei et al., 2010). Systematic errors from in-plane translation experiments are comparable to those reported previously (e.g., mean displacement error is 9 nm or about 0.01 pixels here and in Pitter et al., 2002; Quinta da Fonseca et al., 2005), although random errors are larger (≈ 0.06 pixels for small translations and up to 1.1 pixels for the largest translation; Fig. 8), likely due to increasing (i) variability in specimen illumination, (ii) out-of-plane motion generated by alignment errors between the microscope objective and the specimen, and (iii) lens aberration errors with increasing displacement. Strain errors generated by intentional out-of-plane rigid-body translation are similar to those reported by Lei et al. (2010) (~2000 με), another optical microscale DIC study also performed at 500× magnification.

In addition to tests recommended by iDICs, we characterize strain errors using uniaxial tension experiments as performed in some previous DIC studies (e.g., Sun et al., 1997; Quinta da Fonseca et al., 2005; Pan et al., 2013d). Systematic and random strain errors estimated based on these experiments are each approximately 1000 με. Bias error magnitudes increase slightly with increasing mean strain, possibly due to subtle misalignment of stage and camera axes that generates some off-axis or out-of-plane motion when re-centering the ROI to the field of view. End effects near the clamped portions of the polymer specimen may also increase the strain locally and thereby decrease the true strain

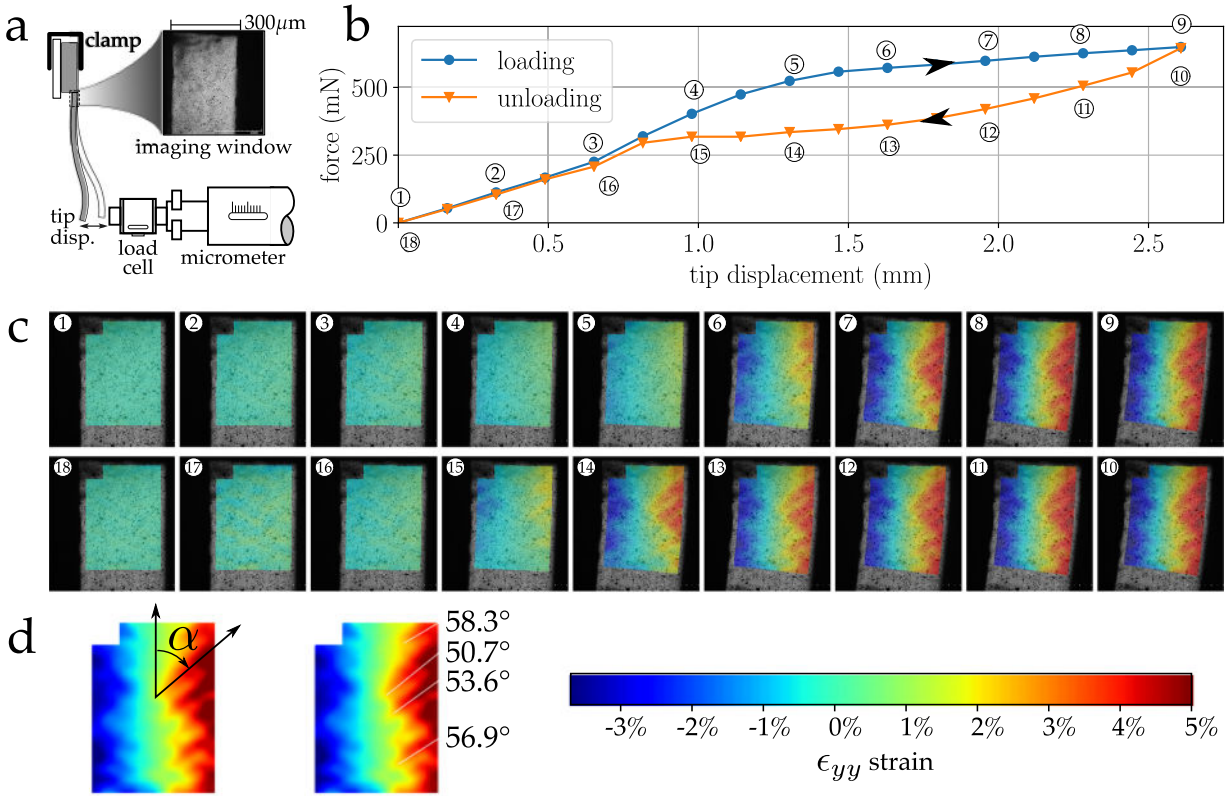

Fig. 10. Representative full-field strain measurements for a nitinol device coupon heated in air to 37 °C. The geometry of the coupon is that of a single strut of a generic IVC filter designed by the authors (Fig. 4). (a) Schematic showing fixed-free cantilever bending boundary conditions applied to the coupon specimens. The free end of the strut is displaced by contact with a non-rotating flat micrometer tip, which is attached to the sensing end of the load cell. (b) Force versus micrometer tip displacement curve during loading and unloading. (c) Full-field strain results mapped to the *deformed* configuration and overlaid on deformed images for loading (①–⑨) and unloading (⑩–⑱). (d) Enlarged view of the full-field strain results mapped to the *reference* configuration with measured transformation band angles. For the specimen shown, the transformation band front angles α are 54.9° ± 3°. All strains are Green–Lagrange.

generated in the observed ROI. In general, strain errors are higher than those typically obtained with macroscale DIC setups (e.g., ≈ 50 $\mu\epsilon$ in Pan et al., 2013d), but are comparable to those reported for previous microscale measurements (e.g., 500 $\mu\epsilon$ in Quinta da Fonseca et al., 2005). The importance of these errors, however, depends on the intended use for the DIC measurements and the associated signal-to-noise ratio for an application (Dickinson et al., 2010). That is, the DIC measurement errors are generally acceptable for an experiment as long as the strains of interest are much greater than the noise floor. Thus, the DIC setup developed herein could reasonably be used for applications where strains of interest are greater than 1000 $\mu\epsilon$ (0.1%) by a factor of two or three.

To demonstrate the characterized microscale 2D-DIC system, we acquire full-field measurements of a single strut of a generic nitinol medical device undergoing emulated physiological and hyperphysiological loading. Inhomogeneous deformations are observed in the form of Lüders-like transformation bands comparable to those previously described during uniaxial extension (Shaw and Kyriakides, 1997; Murasawa et al., 2009; Reedlunn et al., 2014) and four-point bending (Reedlunn et al., 2014; Bechle and Kyriakides, 2014) of superelastic nitinol strips and tubes. As explained by Hill (1952) and later applied to superelastic deformations of nitinol by Shaw and Kyriakides (1997) and Reedlunn et al. (2014), the ideal in-plane band front angle α for necking of a thin strip in uniaxial tension is described by $\cos(2\alpha) = -\frac{1-\nu}{1+\nu}$, where ν is the Poisson's ratio of the material. Assuming no volume change during plastic (here pseudoplastic) deformation such that $\nu = \frac{1}{2}$, the predicted in-plane front angle is $\alpha = 54.74°$. Although experiments here consider cantilever bending rather than uniaxial tension, mapping the strain results to the reference (i.e., undeformed) configuration, the observed transformation band angles of 54.9° ± 3° (Fig. 10) closely agree with the band angle predicted by theory as well as with those reported in previous investigations of nitinol by Shaw and Kyriakides (1997) and Murasawa et al. (2007) (≈55°) and by Reedlunn et al. (2014) (44.5° to 70.5° for tubes in bending).

Some limitations of the microscale 2D-DIC approach described here should be noted. First, magnification and depth of field are inherently limited by the physics of optical microscopy. Both higher magnification and greater depth of field are possible using more advanced techniques such as scanning electron or atomic force microscopy. However, as noted by others (e.g., Quinta da Fonseca et al., 2005; Jonnalagadda et al., 2009), the advantages of these approaches come with the additional cost, setup and acquisition time, and complications such as sensitivity to electrical noise and spatial drift. In the absence of advanced techniques (Pan and Wang, 2013c; Li et al., 2017), measurements acquired using a single camera and single perspective optical microscope are also limited by being strictly two-dimensional and are, thus, subject to out-of-plane errors with even subtle changes in working distance during an experiment. Because of these limitations of 2D-DIC, the iDICs good practices guide states "[s]tereo-DIC is strongly recommended over 2D-DIC for all tests if possible, even tests in which a nominally planar test piece undergoes nominally planar deformation" (Section 2.1.5 in Jones and Iadicola, 2018). However, stereo-DIC has its own challenges at the microscale, for example, physical limitations to the minimum distance at which separate camera sensors can be positioned. Stereomicroscopy is also similarly restricted to small depths of field, making the technique again impractical unless specimens are approximately planar. Indeed, commenting on the relative strengths and weaknesses of 2D versus stereo-DIC, Pan et al. (2009c) predict that 2D-DIC will remain an "effective and irreplaceable tool" for measurement at the microscale for the foreseeable future.

5. Summary and conclusions

- 2D-DIC measurements are demonstrated over sub-millimeter fields of view with sub-micron displacement accuracy using an unmodified digital optical microscope and a simple, inexpensive, and fast speckling technique. A low-cost temperature- and displacement-controlled load frame is also demonstrated that accommodates the short working distances required by high-magnification optical microscopy.
- Following general recommendations from the iDICs good practices guide (Jones and Iadicola, 2018), we performed multiple tests to characterize and estimate the displacement and strain errors associated with our DIC setup. Based on the error characterization experiments, systematic and random errors in strain are each estimated to be approximately 1000 $\mu\epsilon$. The method is thus useful for applications where strains of interest are greater than 1000 $\mu\epsilon$ (0.1%) by a factor of two or three.
- Full-field strain measurements are acquired on the sidewall of a finished laser-cut nitinol medical device coupon with a strut width of approximately 300 μm. Microscale Lüders-like transformation bands are observed in the nitinol strut at larger deformations.
- Future use of microscale DIC in the medical device industry is motivated by the need to (i) validate computational models used in the development and durability assessment of cardiovascular devices, (ii) characterize the mechanics of these devices and detect cyclic phase transformations when present, and (iii) guide the development of next-generation constitutive models for superelasticity and inhomogeneous deformations (e.g., strain localization). The emergence of free and open-source DIC softwares (e.g., `Ncorr` Blaber et al., 2015, `DICe` Turner, 2015, `MultiDIC` Solav et al., 2018, `pyDIC` Belloni et al., 2019) will further drive the adoption of DIC for these applications.

CRediT authorship contribution statement

Kenneth I. Aycock: Conceptualization, Data curation, Formal analysis, Investigation, Methodology, Software, Visualization, Writing - original draft. **Jason D. Weaver:** Conceptualization, Funding acquisition, Methodology, Writing - review & editing. **Harshad M. Paranjape:** Methodology, Resources, Writing - review & editing. **Karthikeyan Senthilnathan:** Methodology, Resources, Writing - review & editing. **Craig Bonsignore:** Methodology, Resources, Writing - review & editing. **Brent A. Craven:** Conceptualization, Funding acquisition, Methodology, Project administration, Writing - review & editing.

Declaration of competing interest

The authors declare that they have no known competing financial interests or personal relationships that could have appeared to influence the work reported in this paper.

Acknowledgments

We thank Daniel Porter (FDA) for reviewing the manuscript. We also thank Andrew Baumann, Maureen Dreher, Shiril Sivan, Daniel Porter (FDA), Tom Duerig (Confluent Medical Technologies), and Robert Campbell (Pennsylvania State University) for helpful discussions. This study was performed under an active Research Collaborative Agreement between FDA and Confluent Medical Technologies and was funded by the U.S. FDA Center for Devices and Radiological Health (CDRH) Critical Path program, United States of America. The research was supported in part by an appointment to the Research Participation Program at the U.S. FDA administered by the Oak Ridge Institute for Science and Education through an interagency agreement between the U.S. Department of Energy and FDA. The findings and conclusions in this article have not been formally disseminated by the U.S. FDA and should not be construed to represent any agency determination or policy. The mention of commercial products, their sources, or their use in connection with material reported herein is not to be construed as either an actual or implied endorsement of such products by the Department of Health and Human Services.

References

ASME V&V 40, 2018. Assessing Credibility of Computational Models through Verification and Validation: Application to Medical Devices. American Society of Mechanical Engineers.

Barranger, Y., Doumalin, P., Dupré, J.C., Germaneau, A., 2012. Strain measurement by digital image correlation: influence of two types of speckle patterns made from rigid or deformable marks. Strain 48 (5), 357–365, [Online]. Available: http://dx.doi.org/10.1111/j.1475-1305.2011.00831.x.

Bay, B.K., Smith, T.S., Fyhrie, D.P., Saad, M., 1999. Digital volume correlation: three-dimensional strain mapping using X-ray tomography. Exp. Mech. 39 (3), 217–226.

Bechle, N.J., Kyriakides, S., 2014. Localization in NiTi tubes under bending. Int. J. Solids Struct. 51 (5), 967–980.

Bechle, N.J., Kyriakides, S., 2016. Evolution of localization in pseudoelastic NiTi tubes under biaxial stress states. Int. J. Plast. 82, 1–31.

Belloni, V., Ravanelli, R., Nascetti, A., Di Rita, M., Mattei, D., Crespi, M., 2019. py2DIC: A new free and open source software for displacement and strain measurements in the field of experimental mechanics. Sensors 19 (18), 3832.

Berfield, T.A., Patel, J.K., Shimmin, R.G., Braun, P.V., Lambros, J., Sottos, N.R., 2007. Micro- and nanoscale deformation measurement of surface and internal planes via digital image correlation. Exp. Mech. 47 (1), 51–62, [Online]. Available: http://dx.doi.org/10.1007/s11340-006-0531-2.

Bewerse, C., Gall, K.R., McFarland, G.J., Zhu, P., Brinson, L.C., 2013. Local and global strains and strain ratios in shape memory alloys using digital image correlation. Mater. Sci. Eng. A 568, 134–142.

Bian, X., Gazder, A.A., Saleh, A.A., Pereloma, E.V., 2019. A comparative study of a NiTi alloy subjected to uniaxial monotonic and cyclic loading-unloading in tension using digital image correlation: the grain size effect. J. Alloys Compd. 777, 723–735.

Blaber, J., Adair, B., Antoniou, A., 2015. Ncorr: open-source 2D digital image correlation Matlab software. Exp. Mech. 55 (6), 1105–1122.

Bradski, G., 2000. The OpenCV library. Dr. Dobb's J. Softw. Tools.

Catoor, D., Ma, Z., Kumar, S., 2019. Cyclic response and fatigue failure of Nitinol under tension–tension loading. J. Mater. Res. 34 (20), 3504–3522, [Online]. Available: http://dx.doi.org/10.1557/jmr.2019.254.

Chu, T.C., Ranson, W.F., Sutton, M.A., 1985. Applications of digital-image-correlation techniques to experimental mechanics. Exp. Mech. 25 (3), 232–244, [Online]. Available: http://dx.doi.org/10.1007/BF02325092.

Daly, S., Ravichandran, G., Bhattacharya, K., 2007. Stress-induced martensitic phase transformation in thin sheets of Nitinol. Acta Mater. 55 (10), 3593–3600.

Davidson, D.L., Williams, D.R., Buckingham, J.E., 1983. Crack-tip stresses as computed from strains determined by stereoimaging. Exp. Mech. 23 (2), 242–248, [Online]. Available: http://dx.doi.org/10.1007/BF02320416.

Dickinson, A.S., Taylor, A.C., Ozturk, H., Browne, M., 2010. Experimental validation of a finite element model of the proximal femur using digital image correlation and a composite bone model. J. Biomech. Eng. 133 (1), [Online]. Available: http://dx.doi.org/10.1115/1.4003129.

Duerig, T., Pelton, A., Bhattacharya, K., 2017. The measurement and interpretation of transformation temperatures in nitinol. Shape Mem. Superelasticity 3 (4), 485–498.

Quinta da Fonseca, J., Mummery, P., Withers, P., 2005. Full-field strain mapping by optical correlation of micrographs acquired during deformation. J. Microsc. 218 (1), 9–21.

Ghosh, R., Gupta, S., Dickinson, A., Browne, M., 2012. Experimental validation of finite element models of intact and implanted composite hemipelvises using digital image correlation. J. Biomech. Eng. 134 (8), 081003.

Gianola, D.S., 2007. Deformation Mechanisms in Nanocrystalline Aluminum Thin Films: An Experimental Investigation (Ph.D. dissertation). Johns Hopkins University.

Gong, J.Y., Daly, S.H., 2016. Microscale repeatability of the shape-memory effect in fine NiTi wires. Shape Mem. Superelasticity 2 (4), 298–309, [Online]. Available: http://dx.doi.org/10.1007/s40830-016-0081-0.

Grassi, L., Väänänen, S.P., Yavari, S.A., Weinans, H., Jurvelin, J.S., Zadpoor, A.A., Isaksson, H., 2013. Experimental validation of finite element model for proximal composite femur using optical measurements. J. Mech. Behav. Biomed. Mater. 21, 86–94.

Hallai, J.F., Kyriakides, S., 2013. Underlying material response for Lüders-like instabilities. Int. J. Plast. 47, 1–12.

Harilal, R., et al., 2014. Adaptation of open source 2D DIC software Ncorr for solid mechanics applications. In: Proceedings of the 9th International Symposium on Advanced Science and Technology in Experimental Mechanics, ISEM '14, New Delhi, 1–6, 2014, November.

Hill, R., 1952. On discontinuous plastic states, with special reference to localized necking in thin sheets. J. Mech. Phys. Solids 1 (1), 19–30.

Jetté, B., Brailovski, V., Simoneau, C., Dumas, M., Terriault, P., 2018. Development and in vitro validation of a simplified numerical model for the design of a biomimetic femoral stem. J. Mech. Behav. Biomed. Mater. 77, 539–550.

Jiang, D., Kyriakides, S., Landis, C.M., 2017a. Propagation of phase transformation fronts in pseudoelastic NiTi tubes under uniaxial tension. Extreme Mech. Lett. 15, 113–121.

Jiang, D., Kyriakides, S., Landis, C.M., Kazinakis, K., 2017b. Modeling of propagation of phase transformation fronts in NiTi under uniaxial tension. Eur. J. Mech. A Solids 64, 131–142.

Jin, H., Lu, W., Korellis, J., 2008. Micro-scale deformation measurement using the digital image correlation technique and scanning electron microscope imaging. J. Strain Anal. Eng. Des. 43 (8), 719–728.

Jones, E., Iadicola, M., 2018. A Good Practices Guide for Digital Image Correlation. Tech. Rep., International Digital Image Correlation Society.

Jonnalagadda, K.N., Chasiotis, I., Yagnamurthy, S., Lambros, J., Pulskamp, J., Polcawich, R., Dubey, M., 2009. Experimental investigation of strain rate dependence of nanocrystalline Pt films. Exp. Mech. 50 (1), 25–35, [Online]. Available: http://dx.doi.org/10.1007/s11340-008-9212-7.

Kammers, A.D., Daly, S., 2013. Digital image correlation under scanning electron microscopy: methodology and validation. Exp. Mech. 53 (9), 1743–1761, [Online]. Available: http://dx.doi.org/10.1007/s11340-013-9782-x.

Kimiecik, M., Jones, J., Daly, S., 2013. Quantitative Studies of microstructural phase transformation in Nickel–Titanium. Mater. Lett. 95, 25–29.

Lagattu, F., Bridier, F., Villechaise, P., Brillaud, J., 2006. In-plane strain measurements on a microscopic scale by coupling digital image correlation and an in situ SEM technique. Mater. Charact. 56 (1), 10–18, [Online]. Available: http://dx.doi.org/10.1016/j.matchar.2005.08.004.

Lecompte, D., Smits, A., Bossuyt, S., Sol, H., Vantomme, J., Van Hemelrijck, D., Habraken, A., 2006. Quality assessment of speckle patterns for digital image correlation. Opt. Lasers Eng. 44 (11), 1132–1145.

Lei, D., Hou, F., Gong, X., 2010. Investigation of deformation at the grain scale in polycrystalline materials by coupling digital image correlation and digital microscopy. Exp. Tech. 36 (2), 24–31, [Online]. Available: http://dx.doi.org/10.1111/j.1747-1567.2010.00670.x.

Li, J., Dan, X., Xu, W., Wang, Y., Yang, G., Yang, L., 2017. 3D digital image correlation using single color camera pseudo-stereo system. Opt. Laser Technol. 95, 1–7, [Online]. Available: http://dx.doi.org/10.1016/j.optlastec.2017.03.030.

Li, N., Sutton, M.A., Li, X., Schreier, H.W., 2007. Full-field thermal deformation measurements in a scanning electron microscope by 2D digital image correlation. Exp. Mech. 48 (5), 635–646, [Online]. Available: http://dx.doi.org/10.1007/s11340-007-9107-z.

Mazière, M., Luis, C., Marais, A., Forest, S., Gaspérini, M., 2017. Experimental and numerical analysis of the Lüders phenomenon in simple shear. Int. J. Solids Struct. 106, 305–314.

Murasawa, G., Kitamura, K., Yoneyama, S., Miyazaki, S., Miyata, K., Nishioka, A., Koda, T., 2009. Macroscopic stress–strain curve, local strain band behavior and the texture of NiTi thin sheets. Smart Mater. Struct. 18 (5), 055003.

Murasawa, G., Yoneyama, S., Sakuma, T., 2007. Nucleation, bifurcation and propagation of local deformation arising in NiTi shape memory alloy. Smart Mater. Struct. 16 (1), 160.

Op Den Buijs, J., Dragomir-Daescu, D., 2011. Validated finite element models of the proximal femur using two-dimensional projected geometry and bone density. Comput. Methods Programs Biomed. 104 (2), 168–174, [Online]. Available: http://dx.doi.org/10.1016/j.cmpb.2010.11.008.

Palanca, M., Tozzi, G., Cristofolini, L., 2015. The use of digital image correlation in the biomechanical area: a review. Int. Biomech. 3 (1), 1–21, [Online]. Available: http://dx.doi.org/10.1080/23335432.2015.1117395.

Pan, B., 2009a. Reliability-guided digital image correlation for image deformation measurement. Appl. Opt. 48 (8), 1535–1542.

Pan, B., 2013a. Bias error reduction of digital image correlation using Gaussian pre-filtering. Opt. Lasers Eng. 51 (10), 1161–1167.

Pan, B., 2018. Digital image correlation for surface deformation measurement: historical developments, recent advances and future goals. Meas. Sci. Technol. 29 (8), 082001.

Pan, B., Asundi, A., Xie, H., Gao, J., 2009b. Digital image correlation using iterative least squares and pointwise least squares for displacement field and strain field measurements. Opt. Lasers Eng. 47 (7–8), 865–874.

Pan, B., Li, K., Tong, W., 2013b. Fast, robust and accurate digital image correlation calculation without redundant computations. Exp. Mech. 53 (7), 1277–1289, [Online]. Available: http://dx.doi.org/10.1007/s11340-013-9717-6.

Pan, B., Lu, Z., Xie, H., 2010a. Mean intensity gradient: an effective global parameter for quality assessment of the speckle patterns used in digital image correlation. Opt. Lasers Eng. 48 (4), 469–477, [Online]. Available: http://dx.doi.org/10.1016/j.optlaseng.2009.08.010.

Pan, B., Qian, K., Xie, H., Asundi, A., 2009c. Two-dimensional digital image correlation for in-plane displacement and strain measurement: a review. Meas. Sci. Technol. 20 (6), 062001.

Pan, B., Wang, Q., 2013c. Single-camera microscopic stereo digital image correlation using a diffraction grating. Opt. Express 21 (21), 25056, [Online]. Available: http://dx.doi.org/10.1364/OE.21.025056.

Pan, B., Xie, H., Wang, Z., 2010b. Equivalence of digital image correlation criteria for pattern matching. Appl. Opt. 49 (28), 5501–5509.

Pan, B., Yu, L., Wu, D., 2013d. High-accuracy 2D digital image correlation measurements with bilateral telecentric lenses: Error analysis and experimental verification. Exp. Mech. 53 (9), 1719–1733, [Online]. Available: http://dx.doi.org/10.1007/s11340-013-9774-x.

Paranjape, H.M., Ng, B., Ong, I., Vien, L., Huntley, C., 2020. Phase transformation volume amplitude as a low-cycle fatigue indicator in nickel–titanium shape memory alloys. Scr. Mater. 178, 442–446.

Paranjape, H.M., Paul, P.P., Sharma, H., Kenesei, P., Park, J.-S., Duerig, T., Brinson, L.C., Stebner, A.P., 2017. Influences of granular constraints and surface effects on the heterogeneity of elastic, superelastic, and plastic responses of polycrystalline shape memory alloys. J. Mech. Phys. Solids 102, 46–66.

Pathmanathan, P., Gray, R.A., Romero, V.J., Morrison, T.M., 2017. Applicability analysis of validation evidence for biomedical computational models. J. Verif. Valid. Uncertain. Quantif. 2 (2), 021005.

Peters, W., Ranson, W., 1982. Digital imaging techniques in experimental stress analysis. Opt. Eng. 21 (3), 213427.

Pitter, M.C., See, C.W., Goh, J.Y., Somekh, M.G., 2002. Focus errors and their correction in microscopic deformation analysis using correlation. Opt. Express 10 (23), 1361–1367.

Reedlunn, B., Churchill, C.B., Nelson, E.E., Shaw, J.A., Daly, S.H., 2014. Tension, compression, and bending of superelastic shape memory alloy tubes. J. Mech. Phys. Solids 63, 506–537.

Reedlunn, B., Daly, S., Hector, L., Zavattieri, P., Shaw, J., 2011. Tips and tricks for characterizing shape memory wire part 5: full-field strain measurement by digital image correlation. Exp. Tech. 37 (3), 62–78, [Online]. Available: http://dx.doi.org/10.1111/j.1747-1567.2011.00717.x.

Reu, P., 2012. Introduction to digital image correlation: best practices and applications. Exp. Tech. 36 (1), 3–4, [Online]. Available: http://dx.doi.org/10.1111/j.1747-1567.2011.00798.x.

Reu, P., 2015. DIC: a revolution in experimental mechanics. Exp. Tech. 39 (6), 1–2.

Reu, P.L., Toussaint, E., Jones, E., Bruck, H.A., Iadicola, M., Balcaen, R., Turner, D.Z., Siebert, T., Lava, P., Simonsen, M., 2018. DIC challenge: developing images and guidelines for evaluating accuracy and resolution of 2D analyses. Exp. Mech. 58 (7), 1067–1099.

Schneider, C.A., Rasband, W.S., Eliceiri, K.W., 2012. NIH Image to ImageJ: 25 years of image analysis. Nat. Methods 9 (7), 671.

Shaw, J.A., Kyriakides, S., 1997. Initiation and propagation of localized deformation in elasto-plastic strips under uniaxial tension. Int. J. Plasticity 13 (10), 837–871.

Solav, D., Moerman, K.M., Jaeger, A.M., Genovese, K., Herr, H.M., 2018. MultiDIC: An open-source toolbox for multi-view 3D digital image correlation. IEEE Access 6, 30520–30535.

Su, Y., Zhang, Q., Gao, Z., Xu, X., Wu, X., 2015. Fourier-based interpolation bias prediction in digital image correlation. Opt. Express 23 (15), 19242, [Online]. Available: http://dx.doi.org/10.1364/OE.23.019242.

Sun, Z., Lyons, J.S., McNeill, S.R., 1997. Measuring microscopic deformations with digital image correlation. Opt. Lasers Eng. 27 (4), 409–428.

Sun, Y., Pang, J.H., 2006. AFM image reconstruction for deformation measurements by digital image correlation. Nanotechnology 17 (4), 933.

Sutradhar, A., Park, J., Carrau, D., Miller, M.J., 2014. Experimental validation of 3D printed patient-specific implants using digital image correlation and finite element analysis. Comput. Biol. Med. 52, 8–17.

Sutton, M., Ke, X., Lessner, S., Goldbach, M., Yost, M., Zhao, F., Schreier, H., 2008a. Strain field measurements on mouse carotid arteries using microscopic three-dimensional digital image correlation. J. Biomed. Mater. Res. A 84A (1), 178–190, [Online]. Available: http://dx.doi.org/10.1002/jbm.a.31268.

Sutton, M.A., Orteu, J.J., Schreier, H., 2009. Image Correlation for Shape, Motion and Deformation Measurements: Basic Concepts, Theory and Applications. Springer Science & Business Media.

Sutton, M., Wolters, W., Peters, W., Ranson, W., McNeill, S., 1983. Determination of displacements using an improved digital correlation method. Image Vis. Comput. 1 (3), 133–139.

Sutton, M.A., Yan, J., Tiwari, V., Schreier, H., Orteu, J.-J., 2008b. The effect of out-of-plane motion on 2D and 3D digital image correlation measurements. Opt. Lasers Eng. 46 (10), 746–757.

Tiossi, R., Vasco, M.A., Lin, L., Conrad, H.J., Bezzon, O.L., Ribeiro, R.F., Fok, A.S., 2013. Validation of finite element models for strain analysis of implant-supported prostheses using digital image correlation. Dent. Mater. 29 (7), 788–796.

Turner, D., 2015. Digital Image Correlation Engine (DICe) Reference Manual. National Technology & Engineering Solutions of Sandia, SAND2015-10606 O.

Vendroux, G., Knauss, W., 1998. Submicron deformation field measurements: Part 2. Improved digital image correlation. Exp. Mech. 38 (2), 86–92.

Winiarski, B., Schajer, G.S., Withers, P.J., 2011. Surface decoration for improving the accuracy of displacement measurements by digital image correlation in SEM. Exp. Mech. 52 (7), 793–804, [Online]. Available: http://dx.doi.org/10.1007/s11340-011-9568-y.

Ya'akobovitz, A., Krylov, S., Hanein, Y., 2010. Nanoscale displacement measurement of electrostatically actuated micro-devices using optical microscopy and digital image correlation. Sensors Actuators A 162 (1), 1–7, [Online]. Available: http://dx.doi.org/10.1016/j.sna.2010.05.014.

Yan, D., Tasan, C.C., Raabe, D., 2015. High resolution in situ mapping of microstrain and microstructure evolution reveals damage resistance criteria in dual phase steels. Acta Mater. 96, 399–409.

Yu, L., Tao, R., Lubineau, G., 2019. Accurate 3D shape, displacement and deformation measurement using a smartphone. Sensors 19 (3), 719, [Online]. Available: http://dx.doi.org/10.3390/s19030719.

Zhang, S., He, Y., 2018. Fatigue resistance of branching phase-transformation fronts in pseudoelastic NiTi polycrystalline strips. Int. J. Solids Struct. 135, 233–244.

Zheng, L., He, Y., Moumni, Z., 2016. Effects of Lüders-like bands on NiTi fatigue behaviors. Int. J. Solids Struct. 83, 28–44.

Zheng, L., He, Y., Moumni, Z., 2017. Investigation on fatigue behaviors of NiTi polycrystalline strips under stress-controlled tension via in-situ macro-band observation. Int. J. Plast. 90, 116–145.

Zhou, S., Zhu, H., Ma, Q., Ma, S., 2020. Heat transfer and temperature characteristics of a working digital camera. Sensors 20 (9), 2561, [Online]. Available: http://dx.doi.org/10.3390/s20092561.